Energy Materials

Article

Stable and efficient seawater splitting on a porous phosphate-intercalated NiFe (oxy)hydroxide@NiMoO₄ core-shell micropillar electrode

Chen Yang[1,2,#], **Nannan Gao**[1,3,#], **Xilong Wang**[1], **Jiajia Lu**[1], **Lijuan Cao**[1,3], **Yadong Li**[1,2], **Han-Pu Liang**[1,2,4]

[1]Qingdao Institute of Bioenergy and Bioprocess Technology, Chinese Academy of Sciences, Qingdao 266101, Shandong, China.
[2]Center of Materials Science and Optoelectronics Engineering, University of Chinese Academy of Sciences, Beijing 100049, China.
[3]Sino-danish college, University of Chinese Academy of Sciences, Beijing 101408, China.
[4]Dalian National Laboratory for Clean Energy, Dalian 116023, Liaoning, China.
[#]Authors contributed equally.

Correspondence to: Prof. Han-Pu Liang, Qingdao Institute of Bioenergy and Bioprocess Technology, Chinese Academy of Sciences, No. 189 Songling Road, Qingdao 266101, Shandong, China. E-mail: lianghp@qibebt.ac.cn

How to cite this article: Yang C, Gao N, Wang X, Lu J, Cao L, Li Y, Liang HP. Stable and efficient seawater splitting on a porous phosphate-intercalated NiFe (oxy)hydroxide@NiMoO₄ core-shell micropillar electrode. *Energy Mater* 2021;1:100015. https://dx.doi.org/10.20517/energymater.2021.16

Abstract

Seawater splitting powered by solar or wind sources is a significant renewable energy storage technology for the production of green hydrogen energy. However, both the chlorine evolution reaction and chloride corrosion are intractable issues in seawater splitting. Here, a porous electrode based on a phosphate-intercalated NiFe (oxy)hydroxide shell coated on a nickel molybdate (NiMoO₄) micropillar core (denoted as P-NiFe@NiMoO₄) is synthesized through an electrochemical oxidation strategy. During the electrochemical oxidation process, the etching of MoO₂ promotes the reconstruction of NiFe (oxy)hydroxide and the formation of porous structures in an alkaline solution. The optimized P-NiFe@NiMoO₄ electrocatalysts afford a low overpotential of 258 mV at a current density of 100 mA/cm² in alkaline seawater. By pairing the anode with a cathode of as-synthesized P-NiMoO, the electrolyzer presents a low voltage of 1.63 V at 100 mA/cm² in alkaline seawater with excellent stability. Moreover, the remarkable stability of the anode seems to be attributed to the *in-situ* phosphate formed during the electrochemical oxidation process to passivate chloride corrosion.

INTRODUCTION

With the depletion of energy resources and environmental destruction, the exploration of new energy sources has become an urgent priority[1-3]. Hydrogen is the optimal clean energy as a result of its high gravimetric energy density (142 MJ/kg) and pollution-free application[4-8]. Although water splitting is an efficient approach to yield hydrogen, the oxygen evolution reaction (OER) represents a bottleneck owing to its sluggish four-electron process[9-14]. Recently, considering the shortage of freshwater, there has been a dramatic increase in interest in seawater splitting because seawater is the most abundant resource globally. Nevertheless, several challenges remain before this technology can become competitive.

Excess chloride anions represent a crucial challenge during seawater splitting and they may occur in the competitive chlorine evolution reaction at the anode[15,16]. In an alkaline solution, the chlorine furthers react with OH^- to form ClO^- with an onset potential that is ~490 mV higher than that of the OER. Hence, the promising overpotential of OER electrocatalysts under high current must be kept well below 490 mV, under which a seawater electrolysis efficiency of 100% can be achieved. Furthermore, the corrosion of catalysts and substrates from aggressive chloride anions in seawater is another challenge and can lead to poor long-term stability[17]. To slow down this corrosion process, it is vital to develop corrosion-resistant electrodes for seawater splitting.

Traditionally, Pt-, Ir- and Ru-based noble metal catalysts are used for water splitting because of their relatively good activity for both the hydrogen evolution reaction (HER) and OER[18-21]. Nevertheless, considering the high cost, scarcity and poor stability of noble metal catalysts, earth-abundant catalysts, such as transition-metal oxides[22,23], (oxy)hydroxides[24-26], phosphides[27-29], nitrides[15,30,31], borides[32], sulfides[33,34] and selenides[35,36], have been used as promising alternatives in recent years. In particular, transition-metal (oxy)hydroxides have attracted considerable attention for seawater electrolysis due to their high activity. For example, a NiFe layered double hydroxide catalyst synthesized by Dionigi *et al.*[37] showed a high overpotential of 359 mV at 10 mA/cm² in a simulated seawater electrolyte. More recently, Kuang *et al.*[17] reported that an anode based on a NiFe hydroxide-coated NiS_x layer could achieve a high current density of 400 mA/cm² at an overpotential of 510 mV, which tremendously boosted the development of hydrogen production. Liu *et al.*[38] recently constructed a Fe-doped NiOOH catalyst by self-reconstruction, which exhibited an overpotential of 292 mV at 100 mA/cm² and excellent stability. Furthermore, the construction of highly efficient seawater splitting electrocatalysts is essential for balancing catalytic activity and stability.

Herein, we report a porous electrode based on a phosphate-intercalated NiFe (oxy)hydroxide shell coated on a nickel molybdate ($NiMoO_4$) micropillar core (denoted as P-NiFe@$NiMoO_4$) on nickel foam (NF) by an electrochemical oxidation strategy for alkaline seawater splitting. The P-NiFe@$NiMoO_4$ core-shell electrode requires low overpotentials of 238 and 258 mV at a current density of 100 mA/cm² in 1 M KOH and 1 M KOH + seawater electrolytes, respectively. Moreover, the overall alkaline seawater splitting electrolyzer, in which P-NiFe@$NiMoO_4$ is coupled with another efficient HER electrode of P-NiMoO, requires a low voltage of 1.63 V at a current density of 100 mA/cm², benefiting from the distinct porosity and large surface area. Along with excellent catalytic performance, the two-electrode electrolyzer also shows superior stability with a slight decrease over 200 h in alkaline seawater at ambient temperature, attributed to the formation of phosphate that intercalates into NiFe (oxy)hydroxide during the reconstruction process to prevent Cl^- corrosion.

EXPERIMENTAL

Reagents

$FeSO_4 \cdot 9H_2O$ [analytical reagent (AR)], $(NH_4)_6Mo_7O_{24} \cdot 4H_2O$ (AR), $Ni(NO_3)_2 \cdot 6H_2O$ (AR), NaH_2PO_2 (AR), KOH (AR), HCl (AR), ethanol (AR) and commercial RuO_2 were purchased from Shanghai Aladdin Biochemical Technology Co., Ltd, China. With a thickness of 1.6 mm and a porosity of ~95%, NF was provided by Suzhou Jiashide Metal Foam Co., Ltd. Deionized (DI) water was obtained from a Millipore Milli-Q purification system.

Preparation of catalysts

Synthesis of FeNiMoO and NiMoO precursors on nickel foam

A piece of NF (2 × 4 cm²) was cleaned by ultrasonication with 2 M HCl for 15 min and the substrate was then washed with ethanol and DI water several times. A mixture of 378.3 mg of $Ni(NO_3)_2 \cdot 6H_2O$, 202 mg of $FeSO_4 \cdot 7H_2O$ and 395.5 mg of $(NH_4)_6Mo_7O_{24} \cdot 4H_2O$ was dissolved in 40 mL of DI water to form a homogeneous solution. The solution and as-prepared NF substrate were then transferred to a 100 mL Teflon-lined stainless-steel autoclave, which was heated at 150 °C for 6 h. After cooling to room temperature naturally, the sample was washed with DI water several times. The NiMoO precursor was prepared similarly without the addition of $FeSO_4 \cdot 9H_2O$.

Synthesis of P-FeNiMoO, P-NiMoO and A-FeNiMoO electrodes

A total of 400 mg of NaH_2PO_2 on porcelain was put upstream of a furnace and the as-prepared FeNiMoO precursor was put downstream. The furnace was heated at 450 °C for 2 h under an N_2 atmosphere. Similarly, the P-NiMoO electrode was synthesized by replacing the FeNiMoO precursor with a NiMoO precursor. The A-FeNiMoO electrode was synthesized by directly annealing the FeNiMoO precursor in a tube furnace. The annealing treatment was conducted at 450 °C for 2 h under an N_2 atmosphere.

Synthesis of P-NiFe@NiMoO₄, A-NiFe@NiMoO₄ and P-Ni@NiMoO₄ electrodes

An electrochemical oxidation process was deployed to synthesize the three electrodes. The P-FeNiMoO, P-NiMoO and A-FeNiMoO electrodes were electroxidized under a current density of 100 mA/cm² for 6 h to obtain P-NiFe@NiMoO₄, P-Ni@NiMoO₄ and A-NiFe@NiMoO₄, respectively.

Preparation of RuO_2 and Pt/C catalysts on carbon paper

To prepare the RuO_2 electrode for comparison, 3 mg of RuO_2 and 10 μL of Nafion were dispersed in 990 μL of ethanol and the mixture was ultrasonicated for 30 min. A 100 μL dispersion was then coated onto a clean carbon paper substrate, where the mass loading was 300 μg/cm², followed by drying in air. Pt/C electrodes were obtained by a similar method but with a mass loading of 30 mg/cm².

Characterization of catalysts

Physical characterization

Scanning electron microscopy (SEM) and energy-dispersive X-ray spectroscopy were performed with a Hitachi S-4800 scanning electron microscope equipped with an energy dispersive X-ray analyzer (HORIBA, 7593-H). Both transmission electron microscopy (TEM) and high-resolution transmission electron microscopy (HRTEM) were performed with a FEI Tecnai T20 microscope. X-ray diffraction (XRD) patterns were collected on a Bruker D8 Advanced diffractometer using a Cu-Kα radiation source in the 2θ range of 10-80°. X-ray photoelectron spectroscopy (XPS) was performed on a K-Alpha X-ray photoelectron spectrometer (Thermo Scientific). Raman spectroscopy was recorded at ambient temperature on a DXR Raman microscope with a 532 nm excitation length.

Electrochemical measurements

The electrochemical performance was tested using an electrochemical workstation (CH Instruments 660E). The two half reactions of the OER and HER were each carried out at ambient temperature (25 °C) in a standard three-electrode system, with the as-prepared electrode, a graphite rod (for the HER) or Pt mesh (for the OER) and a standard Hg/HgO electrode used as the working, counter and reference electrodes, respectively. All the electrode sizes were ~1 cm^{-2} and the potentials were calibrated to the reversible hydrogen electrode with 85% iR compensation if not specified.

OER polarization curve measurements were performed by cyclic voltammetry (CV) at a scan rate of 5 mV/s and stability tests were carried out under 100 mA cm^{-2} in 1 M KOH. The HER polarization curve was collected by linear sweep voltammetry at a scan rate of 5 mV/s and stability tests were carried out under 100 mA cm^{-2} in 1 M KOH. Electrochemical impedance spectroscopy was measured at an overpotential of 270 mV from 0.1 Hz to 100 kHz with an amplitude of 10 mV. C_{dl} was measured by CV in the non-faradaic region.

The two-electrode electrolyzer was constructed by pairing the as-prepared P-NiFe@$NiMoO_4$ with the P-NiMoO electrode as the anode and cathode, respectively. The workstation was used to measure the polarization curves in different electrolytes. The stability test was carried out with a LANHE battery tester working at a constant current density of 100 mA cm^{-2} at 25 °C.

RESULTS AND DISCUSSION

Scheme 1 presents a schematic for the synthesis process of the porous P-NiFe@$NiMoO_4$ core-shell electrode, with NF used as the substrate benefiting from its natural conductivity, high surface area and abundant reserves. Firstly, a hydrothermal method was deployed to synthesize the FeNiMoO precursor. Secondly, the FeNiMoO precursor was put into a tube furnace for phosphorization treatment, followed by an electrochemical oxidation process. As shown in Supplementary Figure 1, the as-synthesized FeNiMoO precursor electrode turned from brown to black after the phosphorization process. It should be noted that the precursor turned from brown to dark yellow after an annealing treatment under an N_2 atmosphere rather than phosphorization. The FeNiMoO precursor was characterized by SEM. In Supplementary Figure 2, it can be seen that the micropillars with smooth surfaces grew well on the NF. After the phosphorization process, shown in Supplementary Figure 3, the smooth surface of the P-FeNiMoO electrode was covered by a shell of dense material. In a control experiment, another electrode was synthesized with a similar procedure but heated at high temperatures without NaH_2PO_2 (denoted as A-FeNiMoO). In contrast, the A-FeNiMoO electrode in Supplementary Figure 4 shows that these micropillars were broken with cracks on the surface, possibly due to the absence of the covering dense material.

To further investigate the dense shell, a SEM image of a cross section of P-FeNiMoO is provided in Figure 1A, which clearly shows that the micropillar presents a core-shell structure. The XRD pattern of P-FeNiMoO is shown in Supplementary Figure 5. It is evident that the diffraction peaks at 26.1°, 36.7° and 53.3° could be indexed to the (110), (-211) and (220) planes of MoO_2 according to the Joint Committee on Powder Diffraction Standards (JCPDS) No. 78-1072 and the diffraction peaks at 14.2°, 25.3°, 28.7°, 32.5° and 47.5° could be assigned to $NiMoO_4$ according to JCPDS No. 86-0361, which indicates the presence of both $NiMoO_4$ and MoO_2. The XRD pattern of A-FeNiMoO was also collected and is shown in Supplementary Figure 5, where the strong peaks could be assigned to $NiMoO_4$. Moreover, a smaller amount of MoO_2 was obtained during the annealing treatment under N_2 compared with the phosphorization process. Therefore, it is envisaged that the MoO_2 is mainly produced from the reaction of PH_3 produced from the decomposition of NaH_2PO_2 with the FeNiMoO precursor in the process of phosphorization, resulting in the
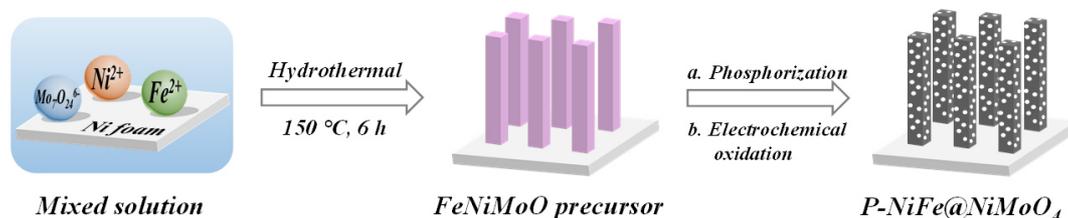
Scheme 1. Schematic of P-NiFe@NiMoO₄ electrode synthesis.
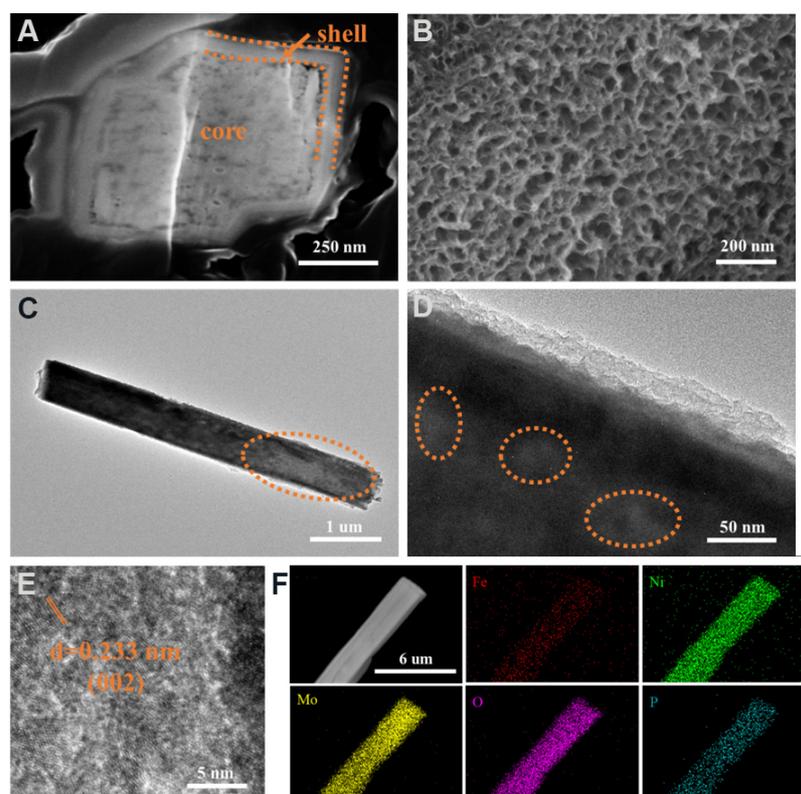
Figure 1. Scanning electron microscopy images of (A) a cross section of P-FeNiMoO and (B) P-NiFe@NiMoO₄ electrode. (C-E) Transmission electron microscopy and high-resolution transmission electron microscopy images of P-NiFe@NiMoO₄ scraped from nickel foam. (F) Elemental mapping images of P-NiFe@NiMoO₄.

formation of the core-shell micropillar structure, as shown in Figure 1A. The core corresponds to $NiMoO_4$ and the shell could be tentatively assigned to a hybrid containing MoO_2 and NiFe phosphorous oxide.

Figure 1B and Supplementary Figure 6 show the SEM images of the P-NiFe@NiMoO₄ electrode at different magnifications, where it is clear that the surface of the micropillars became porous after the electrochemical oxidation process. The numerous pores offer large surface areas, active sites, efficient electrolyte diffusion and oxygen evolution channels. The A-FeNiMoO was electrochemically oxidized using exactly the same process as P-NiFe@NiMoO₄ (denoted as A-NiFe@NiMoO₄). The SEM images in Supplementary Figure 7 show that there is no apparent porous structure on the surface of A-NiFe@NiMoO₄, which further confirms that the formation of the porous structure is closely connected with the etching of MoO_2. The XRD pattern of P-NiFe@NiMoO₄ in Supplementary Figure 5 shows the absence of diffraction peaks associated with MoO_2 after the electrochemical oxidation process in comparison with that of P-FeNiMoO. It has been

reported that low-valence MoO_2 can be oxidized to high-valence MoO_3, which could then be dissolved in an alkaline solution owing to the instability of MoO_3[39,40]. Thus, the emergence of pores could be attributed to the etching of MoO_2, which boosts the reconstruction of the shell during electrochemical oxidation[41], leading to the formation of the porous phosphate-intercalated NiFe (oxy)hydroxide shell.

To gain insights into the electrochemical oxidation process, *in-situ* Raman spectroscopy, as shown in Supplementary Figure 8, was conducted to investigate the surface reconstruction of the catalytic electrode with controlled potentials. For the pristine P-NiFe@NiMoO$_4$ without any potential, the Raman bands at 704, 905 and 950 cm^{-1} can be assigned to the Mo-O vibrations in the MoO_4^{2-} anions, while the bands at 196 and 344 cm^{-1} are assigned to the Mo-O vibrations in MoO_2[42]. The Raman bands are stable and show a minor change when the potential is increased to 1.6 V. With the applied potential increased to 1.8 V, the MoO_2 bands disappear while the NiFe (oxy)hydroxide bands appear at 465 and 545 cm^{-1}, indicating the formation of NiFe (oxy)hydroxide under anodic potentials. The inner $NiMoO_4$ remained stable even when the potential was increased to 2.2 V, in agreement with the literature[41]. It is evidenced that the surface reconstruction contributes to the porous structure.

Figure 1C and D and Supplementary Figure 9 show the TEM images. It is clear from the TEM image in Figure 1D that the pores, indicated by the orange ellipses, are present on the micropillar. It should be noted from the TEM image in Figure 1C that a hollow structure at the lower end of the micropillar, indicated by the orange ellipse, could be tentatively attributed to the fact that the significantly greater amount of PH_3 gas produced during the decomposition of NaH_2PO_2 could react with the FeNiMoO precursor to generate a large amount of MoO_2, the etching of which leads to the formation of the hollow structure instead of pores. The HRTEM image in Figure 1E reveals that the lattice distance of 0.233 nm could be attributed to the (002) plane of $Ni(OH)_2$. The elemental mapping images and composition analysis of P-NiFe@NiMoO$_4$ from energy-dispersive X-ray spectroscopy in Figure 1F and Supplementary Figure 10, respectively, confirm that the Fe, Ni, Mo, O and P elements are uniformly distributed.

The XPS surveys of the P-NiFe@NiMoO$_4$ and P-FeNiMoO electrodes are shown in Figure 2A and Supplementary Figure 11, respectively, which further validate the existence of the Fe, Ni, Mo, O and P elements. Their contents are summarized in Supplementary Table 1. The decrease in Mo content from 7.23% to 0.36% proves the etching of MoO_2 during the electrochemical oxidation process. It can be seen in Figure 2B that the two peaks located at 712.2 and 724.3 eV are assigned to the $2p_{3/2}$ and $2p_{1/2}$ levels of Fe(III), respectively, indicating the presence of the Fe^{3+} oxidation state[43]. The peak at 705.2 eV is assigned to Ni Auger electrons.

The high-resolution X-ray photoelectron spectrum of Ni 2p in Figure 2C demonstrates not only that the peaks located at 872.9 and 855.2 eV are from $Ni(OH)_2$ with a binding energy gap of 17.7 eV[44,45] but also that the peaks located at 875.5 and 856.9 eV from $NiMoO_4$ are observed[46]. In addition, the spectrum of Mo 3d in Figure 2D shows that the two peaks at 235.6 and 232.4 eV belong to Mo^{6+}, thereby further confirming the presence of the inside core of $NiMoO_4$ after the electrochemical oxidation process based on the presence of Ni^{2+} in Figure 2C[47]. The low valence of Mo is shown in Supplementary Figure 12A, which is consistent with the above TEM image and XRD results. As for the O 1s spectrum [Figure 2E], the three peaks at 532.9, 530.9 and 528.9 eV are assigned to H-O-H, metal-OH and metal-O, respectively[48]. The strong P-O peak at 134.3 eV in the P 2p spectrum [Figure 2F] is assigned to the presence of phosphate[49]. Nevertheless, the P-O peak at 133.5 eV in Supplementary Figure 12B negatively shifts, which indeed confirms the formation of NiFe phosphorous oxide after phosphorization. In summary, a porous phosphate-intercalated NiFe (oxy)hydroxide shell covered on $NiMoO_4$, which consists of $Ni(OH)_2$ and FeOOH, appears to have been
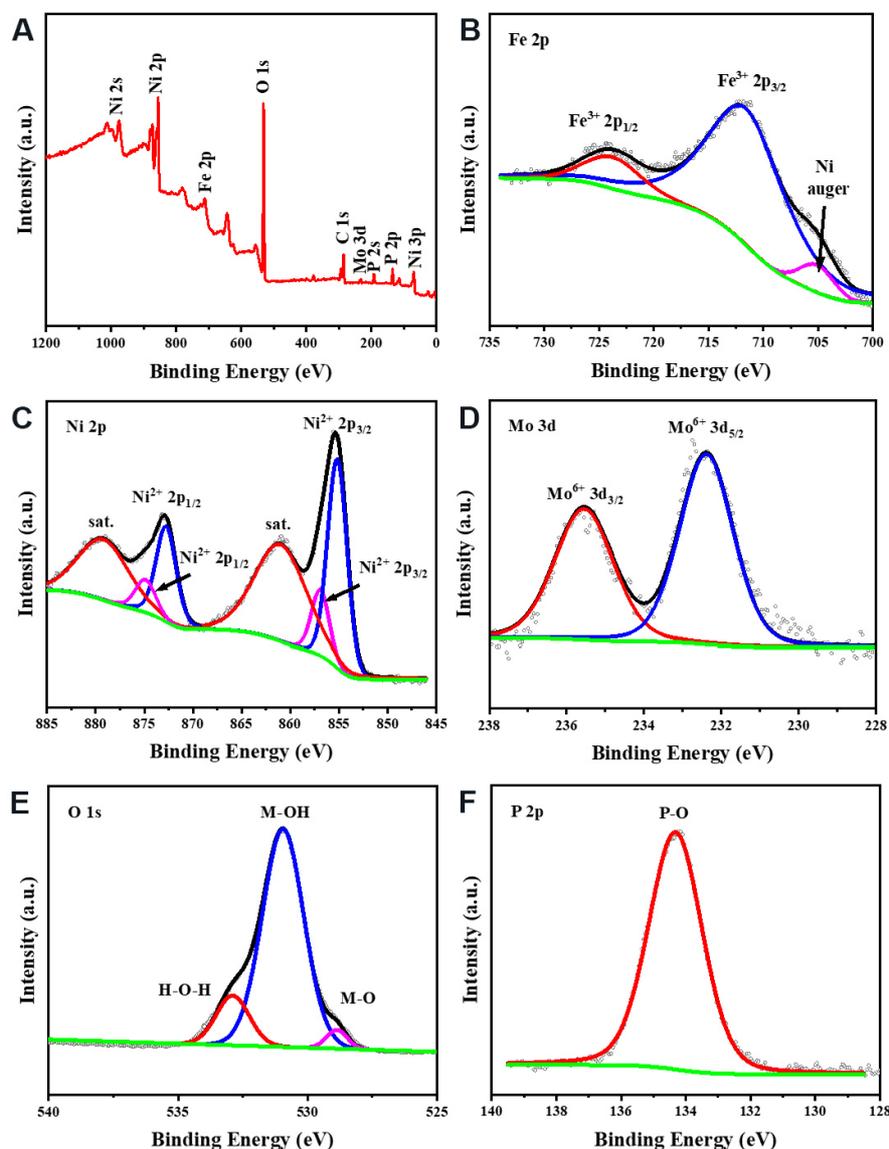
Figure 2. (A) X-ray photoelectron spectroscopy survey and high-resolution spectra of (B) Fe 2p, (C) Ni 2p, (D) Mo 3d, (E) O 1s and (F) P 2p for P-NiFe@NiMoO$_4$ electrode.

formed through a surface reconstruction during the electrochemical oxidation process under high potentials.

To evaluate the OER performance of the P-NiFe@NiMoO$_4$ catalysts, a three-electrode system was deployed in 1 M KOH. A-NiFe@NiMoO$_4$, P-Ni@NiMoO$_4$ and commercial RuO$_2$ were also used as benchmarks for comparison. From the polarization curves shown in Figure 3A and Supplementary Figure 13, it can be seen that the P-NiFe@NiMoO$_4$ electrode exhibits a significant improvement for the OER, compared with A-NiFe@NiMoO$_4$ and P-Ni@NiMoO$_4$ and commercial RuO$_2$. Figure 3B delivers current densities of 100 and 200 mA/cm^2 at small overpotentials of 238 and 257 mV in 1 M KOH, respectively. In addition, even at a higher current density of 300 mA/cm^2, the required overpotential is 266 mV. The overpotential of the P-NiFe@NiMoO$_4$ electrode is well below that of the other as-synthesized electrodes, such as A-NiFe@NiMoO$_4$ and P-Ni@NiMoO$_4$, despite the different current densities. The above results further confirm that the
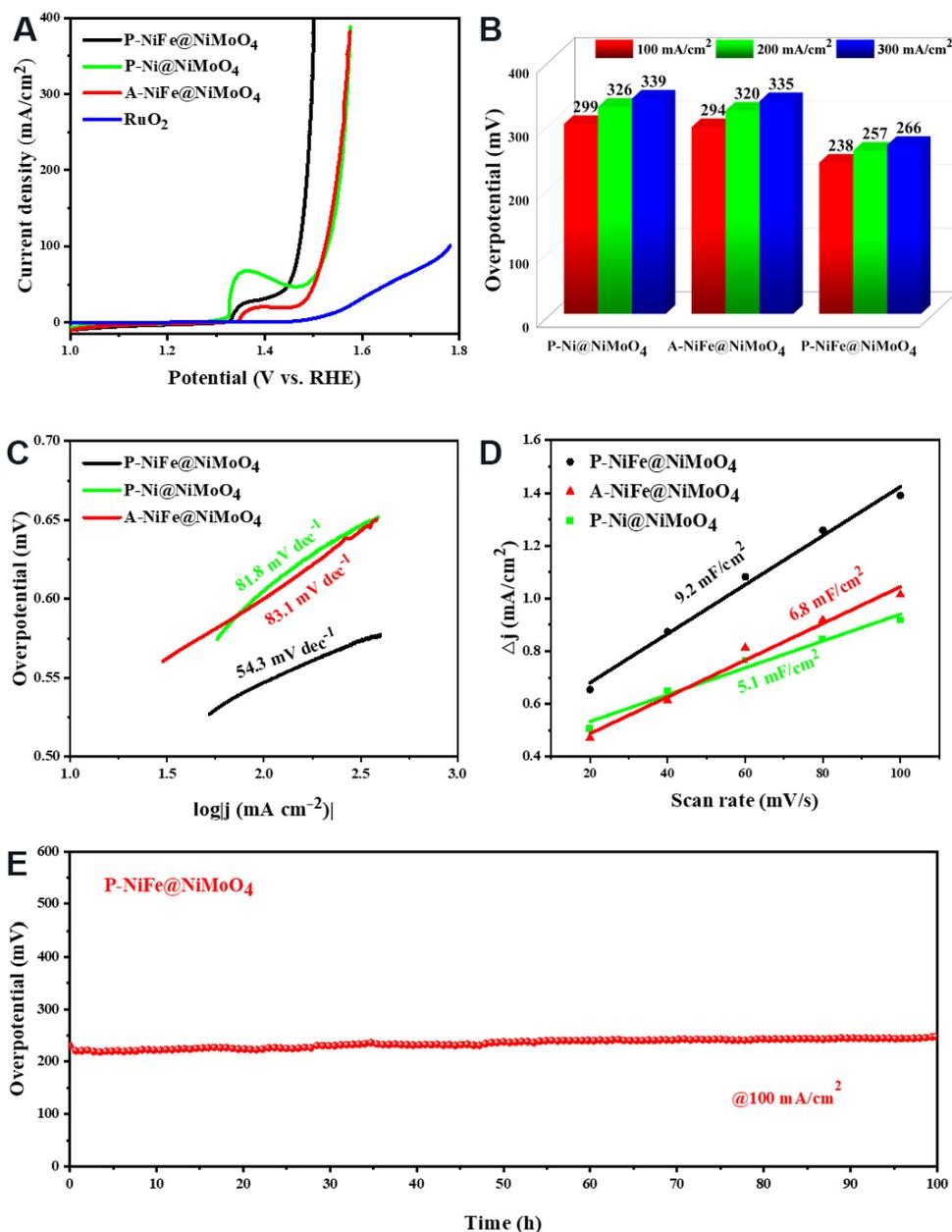
Figure 3. (A) Polarization curves and (B) comparison of overpotentials required to achieve current densities of 100, 200 and 300 mA cm^{-2} of P-NiFe@NiMoO$_4$, A-NiFe@NiMoO$_4$ and P-Ni@NiMoO$_4$ electrodes and commercial RuO$_2$ for the oxygen evolution reaction in 1 M KOH. Corresponding (C) C$_{dl}$ values and (D) Tafel plots of the above electrodes. (E) Chronopotentiometric curve of P-NiFe@NiMoO$_4$ electrode at a current density of 100 mA cm^{-2} in 1 M KOH.

introduction of Fe and P plays a vital part in enhancing the OER performance. Notably, the P element is oxidized to phosphate, which intercalates into the NiFe (oxy)hydroxide layer to resist corrosion from Cl$^-$.

The Tafel plot in Figure 3C shows that the P-NiFe@NiMoO$_4$ electrode exhibits a smaller Tafel slope (54.3 mV/dec) compared with A-NiFe@NiMoO$_4$ (83.1 mV/dec) and P-Ni@NiMoO$_4$ (81.8 mV/dec), suggesting its rapid electrocatalytic kinetics. The high electrochemically active surface area is positively related to the number of active sites, which is calculated from the double-layer capacitance (C$_{dl}$). Figure 3D

presents the C_{dl} values from the CV curves [Supplementary Figure 14]. The C_{dl} values of the P-NiFe@NiMoO$_4$, A-NiFe@NiMoO$_4$ and P-Ni@NiMoO$_4$ electrodes are 9.2, 6.8 and 5.1 mF/cm^2, respectively, implying the highly enhanced surface area and growing active sites implemented by forming the porous NiFe (oxy)hydroxide shell coated on the NiMoO$_4$ micropillars. Electrochemical impedance spectroscopy [Supplementary Figure 15] shows that the charge-transfer resistance (R_{ct}) of the P-NiFe@NiMoO$_4$ electrode is minor (0.11 Ω) compared with A-NiFe@NiMoO$_4$ (0.19 Ω) and P-Ni@NiMoO$_4$ (0.51 Ω), thereby validating its outstanding electronic conductivity and charge transfer. Therefore, the improved OER activity benefits from the large surface area and efficient charge transfer of the porous shell on the NiMoO$_4$ micropillars. Stability is another important parameter that is assessed by chronopotentiometric measurements of the P-NiFe@NiMoO$_4$ electrode at a current density of 100 mA/cm^2 in 1 M KOH at 25 °C. The chronopotentiometric curve of the P-NiFe@NiMoO$_4$ electrode at a current density of 100 mA cm^{-2} in 1 M KOH in Figure 3E indicates that the electrochemical catalytic activity remains constant over 100 h without a noticeable decrease.

An efficient HER catalyst based on the P-NiMoO electrode [Supplementary Figures 16 and 17] was also successfully synthesized to combine with the P-NiFe@NiMoO$_4$ electrode for overall seawater splitting. The HER performance of the P-NiMoO, P-FeNiMoO and A-NiMoO electrodes and commercial Pt/C were tested in 1 M KOH. Supplementary Figure 18A shows that the P-NiMoO electrode could deliver similar overpotentials to the P-FeNiMoO electrode below a current density of 50 mA/cm^2 while exhibiting superior performance above 50 mA/cm^2. The overpotential of the P-NiMoO electrode is only 149 mV at a current density of 100 mA/cm^2, which is higher than that of the A-NiMoO and P-FeNiMoO electrodes. Supplementary Figure 18B and C show that the P-NiMoO electrode presents a smaller Tafel slope of 53 mV/dec and R_{ct} of 0.7 Ω. The C_{dl} value [Supplementary Figure 18D] of the P-NiMoO electrode is 1.076 mF/cm^2, calculated from the CV plots [Supplementary Figure 19]. Moreover, the stability test was carried out in 1 M KOH at a current density of 100 mA/cm^2 and the result demonstrates no significant decrease over 100 h [Supplementary Figure 20].

The OER and HER activities of the P-NiFe@NiMoO$_4$ and P-NiMoO electrodes were then evaluated in simulated seawater (1 M KOH + 0.5 M NaCl) and alkaline seawater (1 M KOH + seawater). The polarization curves in Figure 4A show that the P-NiFe@NiMoO$_4$ electrode retains superior OER activity in 1 M KOH + 0.5 M NaCl, requiring overpotentials of 258, 290 and 312 mV to achieve 100, 200 and 300 mA/cm^2, respectively [Figure 4B]. Moreover, in 1 M KOH + seawater, the activity decreases slightly owing to some insoluble precipitate[16,28]. Even in this situation, the overpotentials of the P-NiFe@NiMoO$_4$ electrode, at current densities of 100, 200 and 300 mA/cm^2, are still 258, 291 and 317 mV, respectively, which surpass those of most reported catalysts [Supplementary Table 2]. Furthermore, the HER activity of the P-NiMoO electrode was also tested in 1 M KOH + 0.5 M NaCl and 1 M KOH + seawater, which requires a similar overpotential of 146 mV at a current density of 100 mA/cm^2 [Supplementary Figure 21].

A two-electrode electrolyzer was set up to further investigate the overall seawater splitting performance in different electrolytes [Figure 4C], where the P-NiFe@NiMoO$_4$ electrode (anode) was coupled with the P-NiMoO electrode (cathode). Remarkably, this electrolyzer exhibits outstanding performance with a low cell voltage of ~1.63 V under a current density of 100 mA/cm^2 in both the 1 M KOH + 0.5 M NaCl and 1 M KOH + seawater electrolytes. Even at larger current densities, the performance is still impressive, outperforming most previously reported electrolyzers [Supplementary Table 3]. The Faradaic efficiency was then evaluated in 1 M KOH + seawater by collecting the evolved H$_2$ and O$_2$ gases [Supplementary Figure 22]. As shown in Figure 4D, the molar ratio of H$_2$ to O$_2$ approaches 2:1 and the measured gas volume is in good agreement with the calculated volume, presenting high Faradaic efficiency
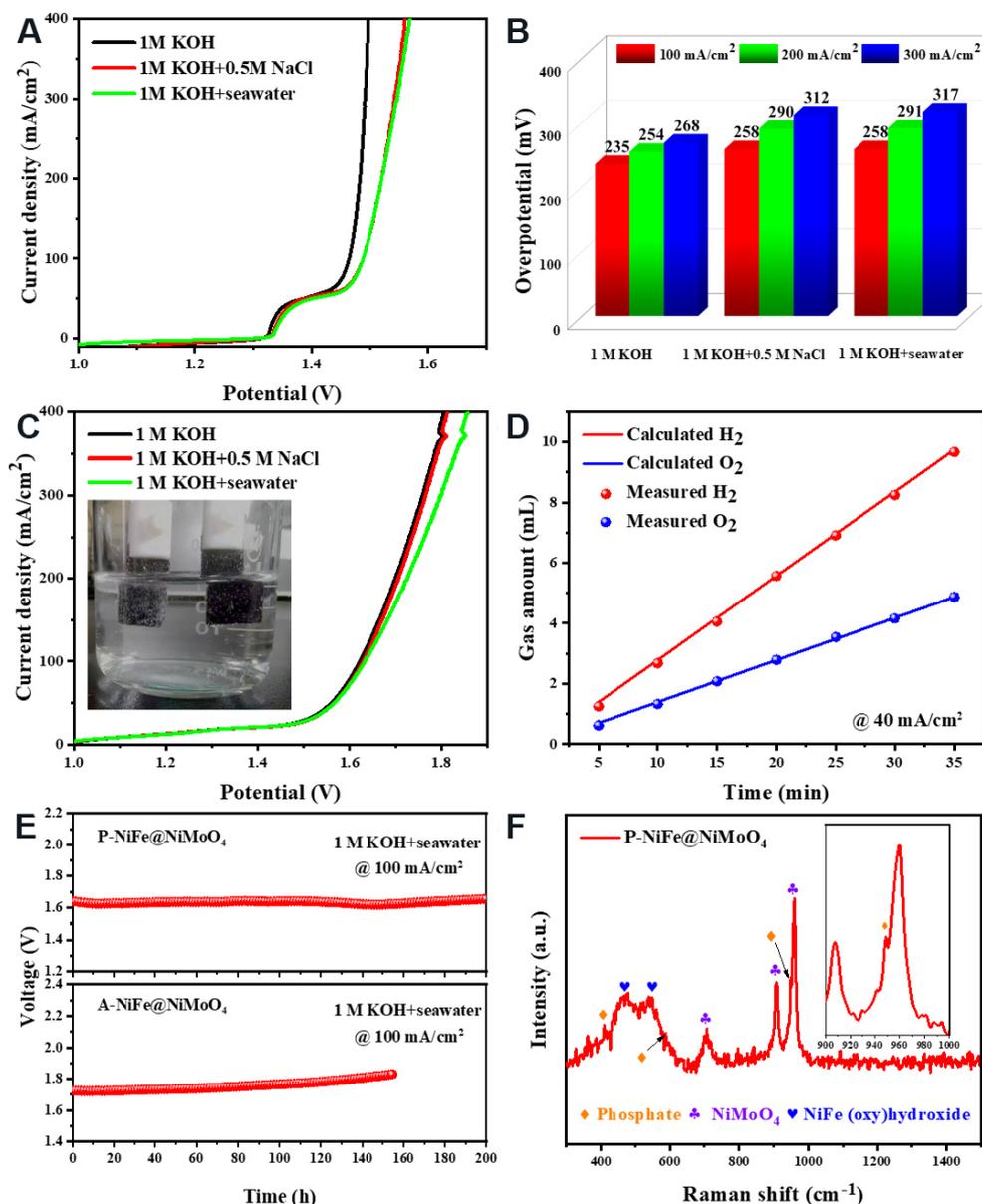
Figure 4. (A) Polarization curves and (B) comparison of overpotentials at different current densities of 100, 200 and 300 mA cm^{-2} of P-NiFe@NiMoO$_4$ electrode tested in different electrolytes. (C) Overall seawater spilling polarization curves in different electrolytes. Inset illustrates the overall two-electrode seawater splitting electrolyzer that paired P-NiFe@NiMoO$_4$ with P-NiMoO. (D) Comparison between the amount of collected and theoretical gaseous products (H$_2$ and O$_2$) by the two-electrode electrolyzer at a constant current density of 40 mA cm^{-2} in 1 M KOH + seawater at 25 °C. (E) Durability tests of electrolyzer at a constant current density of 100 mA cm^{-2} in 1 M KOH + seawater at 25 °C. (F) Raman spectra of P-NiFe@NiMoO$_4$.

and selectivity. Moreover, the as-synthesized P-NiFe@NiMoO$_4$ ‖ P-NiMoO electrolyzer presents excellent stability over 200 h in 1 M KOH + seawater [Figure 4E], while the stability of the A-NiFe@NiMoO$_4$ ‖ P-NiMoO electrolyzer decreases dramatically, indicating the promotion of stability in the presence of phosphate.

For further clarification of phosphate in the P-NiFe@NiMoO$_4$ electrode, Raman spectroscopy [Figure 4F] was conducted, notably showing the presence of phosphate with peaks at 409.8, 588.2 and 948.8 cm^{-1}

assigned to P-O vibrations[50]. The other two strong peaks, at 465.7 and 540.9 cm^{-1}, are assigned to NiFe (oxy)hydroxide[17]. Peaks of MoO_4^{2-} located at 706.8, 907.4 and 960.4 cm^{-1} can also be observed, which is consistent with the XRD result, confirming the $NiMoO_4$ micropillars anchored on the NF substrate[39].

The morphology of the P-NiFe@$NiMoO_4$ electrode after seawater splitting was investigated by SEM [Supplementary Figure 23]. After 200 h of electrolysis, the $NiMoO_4$ micropillars still maintain their initial structure of being firmly anchored on the NF. On the surface of the $NiMoO_4$ micropillars, nanoarrays were formed due to the reconstruction of the Ni and Fe elements during long-term stability under a high potential. Overall, the P-NiFe@$NiMoO_4$ || P-NiMoO electrolyzer works well and delivers a superior cell voltage, indicating its potential application in hydrogen production.

CONCLUSIONS

In summary, we have successfully demonstrated the use of a porous anode made up of phosphate-intercalated NiFe (oxy)hydroxide@$NiMoO_4$ core-shell micropillars for active and stable seawater splitting. The introduction of Fe and the phosphorization are incredibly beneficial to the enhancement of activity and stability. During electrochemical oxidation, the etching of MoO_2 results in a reconstruction process on the micropillars' surface, which generates a porous phosphate-intercalated NiFe (oxy)hydroxide shell. The large pores endow the P-NiFe@$NiMoO_4$ electrode with a large surface area, numerous active sites and efficient charge transfer. The P-NiFe@$NiMoO_4$ electrode exhibits a low overpotential of 258 mV at a current density of 100 mA/cm^2 in alkaline seawater. In addition, by pairing the anode with a P-NiMoO cathode, the two-electrode electrolyzer outputs a current density of 100 mA/cm^2 at a low voltage of 1.63 V. The electrolyzer also exhibits superior stability over 200 h without any apparent activity loss, which is attributed to the passivating anions of phosphate against chloride corrosion. This work provides insight into the development of the industrial application of seawater splitting for green hydrogen production.

DECLARATIONS

Authors' contributions
Methodology, investigation, formal analysis, writing manuscript, visualization: Yang C, Gao N
Validation, resources, formal analysis: Wang X
Validation, investigation: Lu J, Li Y
Formal analysis, validation: Cao L
Project administration, conceptualization, funding acquisition, supervision, writing manuscript: Liang HP

Availability of data and materials
The data supporting our findings can be found in the supplementary information.

Conflicts of interest
All authors declared that there are no conflicts of interest.

Ethical approval and consent to participate

Not applicable.

Consent for publication

Not applicable.

Copyright

© The Author(s) 2021.

REFERENCES

1. Cox CR, Lee JZ, Nocera DG, Buonassisi T. Ten-percent solar-to-fuel conversion with nonprecious materials. *Proc Natl Acad Sci U S A* 2014;111:14057-61. DOI PubMed PMC
2. Faber MS, Jin S. Earth-abundant inorganic electrocatalysts and their nanostructures for energy conversion applications. *Energy Environ Sci* 2014;7:3519-42. DOI
3. Wang X, Yang C, Wang X, et al. Green synthesis of a highly efficient and stable single-atom iron catalyst anchored on nitrogen-doped carbon nanorods for the oxygen reduction reaction. *ACS Sustainable Chem Eng* 2021;9:137-46. DOI
4. Tiwari JN, Sultan S, Myung CW, et al. Multicomponent electrocatalyst with ultralow Pt loading and high hydrogen evolution activity. *Nat Energy* 2018;3:773-82. DOI
5. Turner JA. Sustainable hydrogen production. *Science* 2004;305:972-4. DOI PubMed
6. Cabán-Acevedo M, Stone ML, Schmidt JR, et al. Efficient hydrogen evolution catalysis using ternary pyrite-type cobalt phosphosulphide. *Nat Mater* 2015;14:1245-51. DOI PubMed
7. Luo J, Im JH, Mayer MT, et al. Water photolysis at 12.3% efficiency via perovskite photovoltaics and Earth-abundant catalysts. *Science* 2014;345:1593-6. DOI PubMed
8. Pu Z, Zhao J, Amiinu IS, et al. A universal synthesis strategy for P-rich noble metal diphosphide-based electrocatalysts for the hydrogen evolution reaction. *Energy Environ Sci* 2019;12:952-7. DOI
9. Zhang J, Zhang Q, Feng X. Support and interface effects in water-splitting electrocatalysts. *Adv Mater* 2019;31:e1808167. DOI PubMed
10. Seh ZW, Kibsgaard J, Dickens CF, Chorkendorff I, Nørskov JK, Jaramillo TF. Combining theory and experiment in electrocatalysis: insights into materials design. *Science* 2017;355:eaad4998. DOI PubMed
11. Du J, Li C, Wang X, Shi X, Liang HP. Electrochemical synthesis of cation vacancy-enriched ultrathin bimetallic oxyhydroxide nanoplatelets for enhanced water oxidation. *ACS Appl Mater Interfaces* 2019;11:25958-66. DOI PubMed
12. Li W, Li F, Yang H, et al. A bio-inspired coordination polymer as outstanding water oxidation catalyst via second coordination sphere engineering. *Nat Commun* 2019;10:5074. DOI PubMed PMC
13. Shi Q, Zhu C, Du D, Lin Y. Robust noble metal-based electrocatalysts for oxygen evolution reaction. *Chem Soc Rev* 2019;48:3181-92. DOI PubMed
14. Yu L, Zhou H, Sun J, et al. Amorphous NiFe layered double hydroxide nanosheets decorated on 3D nickel phosphide nanoarrays: a hierarchical core-shell electrocatalyst for efficient oxygen evolution. *J Mater Chem A* 2018;6:13619-23. DOI
15. Yu L, Zhu Q, Song S, et al. Non-noble metal-nitride based electrocatalysts for high-performance alkaline seawater electrolysis. *Nat Commun* 2019;10:5106. DOI PubMed PMC
16. Tong W, Forster M, Dionigi F, et al. Electrolysis of low-grade and saline surface water. *Nat Energy* 2020;5:367-77. DOI
17. Kuang Y, Kenney MJ, Meng Y, et al. Solar-driven, highly sustained splitting of seawater into hydrogen and oxygen fuels. *Proc Natl Acad Sci U S A* 2019;116:6624-9. DOI PubMed PMC
18. Lv F, Zhang W, Yang W, et al. Ir-based alloy nanoflowers with optimized hydrogen binding energy as bifunctional electrocatalysts for overall water splitting. *Small Methods* 2020;4:1900129. DOI
19. Dong J, Duan L, Wu Q, Yao W. Facile preparation of Pt/CdS photocatalyst by a modified photoreduction method with efficient hydrogen production. *Int J Hydrogen Energy* 2018;43:2139-47. DOI
20. Liu S, Huang S. The role of interface charge transfer on Pt based catalysts for water splitting. *Int J Hydrogen Energy* 2018;43:15225-33. DOI
21. Badiei YM, Xie Y, Renderos G, et al. Rapid identification of homogeneous O_2 evolution catalysts and comparative studies of Ru(II)-carboxamides vs. Ru(II)-carboxylates in water-oxidation. *J Catal* 2019;369:10-20. DOI
22. Duan Y, Yu Z, Hu S, et al. Scaled-up synthesis of amorphous NiFeMo oxides and their rapid surface reconstruction for superior oxygen evolution catalysis. *Angew Chem* 2019;131:15919-24. DOI PubMed
23. Wu T, Sun S, Song J, et al. Iron-facilitated dynamic active-site generation on spinel $CoAl_2O_4$ with self-termination of surface reconstruction for water oxidation. *Nat Catal* 2019;2:763-72. DOI
24. Du J, Li C, Wang X, Jones TG, Liang H. Cobalt oxyhydroxide with highly porous structures as active and stable phase for efficient water oxidation. *Electrochimica Acta* 2019;303:231-8. DOI
25. Chen G, Du J, Wang X, Shi X, Wang Z, Liang H. Iron-induced 3D nanoporous iron-cobalt oxyhydroxide on carbon cloth as a highly efficient electrode for oxygen evolution reaction. *Chinese J Catal* 2019;40:1540-7. DOI
26. Huang Z, Song J, Du Y, et al. Chemical and structural origin of lattice oxygen oxidation in Co-Zn oxyhydroxide oxygen evolution

electrocatalysts. *Nat Energy* 2019;4:329-38. DOI

27.   Lv Q, Han J, Tan X, Wang W, Cao L, Dong B. Featherlike NiCoP holey nanoarrys for efficient and stable seawater splitting. *ACS Appl Energy Mater* 2019;2:3910-7. DOI

28.   Wang S, Yang P, Sun X, et al. Synthesis of 3D heterostructure Co-doped Fe_2P electrocatalyst for overall seawater electrolysis. *Applied Catalysis B: Environmental* 2021;297:120386. DOI

29.   Wu L, Yu L, Zhang F, et al. Heterogeneous bimetallic phosphide Ni_2P-Fe_2P as an efficient bifunctional catalyst for water/seawater splitting. *Adv Funct Mater* 2021;31:2006484. DOI

30.   Jin H, Liu X, Vasileff A, et al. Single-crystal nitrogen-rich two-dimensional Mo_5N_6 nanosheets for efficient and stable seawater splitting. *ACS Nano* 2018;12:12761-9. DOI PubMed

31.   Wang B, Lu M, Chen D, et al. $Ni_xFe_yN@C$ microsheet arrays on Ni foam as an efficient and durable electrocatalyst for electrolytic splitting of alkaline seawater. *J Mater Chem A* 2021;9:13562-9. DOI

32.   Gupta S, Forster M, Yadav A, Cowan AJ, Patel N, Patel M. Highly efficient and selective metal oxy-boride electrocatalysts for oxygen evolution from alkali and saline solutions. *ACS Appl Energy Mater* 2020;3:7619-28. DOI

33.   Li Y, Wu X, Wang J, et al. Sandwich structured Ni3S2-MoS2-Ni3S2@Ni foam electrode as a stable bifunctional electrocatalyst for highly sustained overall seawater splitting. *Electrochimica Acta* 2021;390:138833. DOI

34.   Wang C, Zhu M, Cao Z, et al. Heterogeneous bimetallic sulfides based seawater electrolysis towards stable industrial-level large current density. *Applied Catalysis B: Environmental* 2021;291:120071. DOI

35.   Chang J, Wang G, Yang Z, et al. Dual-doping and synergism toward high-performance seawater electrolysis. *Adv Mater* 2021;33:e2101425. DOI PubMed

36.   Hung W, Xue B, Lin T, Lu S, Tsao I. A highly active selenized nickel-iron electrode with layered double hydroxide for electrocatalytic water splitting in saline electrolyte. *Mater Today Energy* 2021;19:100575. DOI

37.   Dionigi F, Reier T, Pawolek Z, Gliech M, Strasser P. Design criteria, operating conditions, and nickel-iron hydroxide catalyst materials for selective seawater electrolysis. *ChemSusChem* 2016;9:962-72. DOI PubMed

38.   Liu J, Ding P, Zhu Z, et al. Engineering self-reconstruction via flexible components in layered double hydroxides for superior-evolving performance. *Small* 2021;17:e2101671. DOI PubMed

39.   Wang W, Yang Z, Jiao F, Gong Y. (P, W)-codoped MoO_2 nanoflowers on nickel foam as an efficient bifunctional electrocatalyst for overall water splitting. *Appl Surf Sci* 2020;529:146987. DOI

40.   Xu C, Lu W, Yan L, et al. Hierarchical molybdenum-doped cobaltous hydroxide nanotubes assembled by cross-linked porous nanosheets with efficient electronic modulation toward overall water splitting. *J Colloid Interface Sci* 2020;562:400-8. DOI PubMed

41.   Solomon G, Landström A, Mazzaro R, et al. $NiMoO_4@Co_3O_4$ core-shell nanorods: in situ catalyst reconstruction toward high efficiency oxygen evolution reaction. *Adv Energy Mater* 2021;11:2101324. DOI

42.   Zhang C, Lu J, Li M, et al. Transfer hydrogenation of nitroarenes with hydrazine at near-room temperature catalysed by a MoO_2 catalyst. *Green Chem* 2016;18:2435-42. DOI

43.   Yu L, Wu L, Mcelhenny B, et al. Ultrafast room-temperature synthesis of porous S-doped Ni/Fe (oxy)hydroxide electrodes for oxygen evolution catalysis in seawater splitting. *Energy Environ Sci* 2020;13:3439-46. DOI

44.   Xiong K, Huang L, Gao Y, et al. Formation of a thin-layer of nickel hydroxide on nickel phosphide nanopillars for hydrogen evolution. *Electrochem commun* 2018;92:9-13. DOI

45.   Wu J, Subramaniam J, Liu Y, Geng D, Meng X. Facile assembly of $Ni(OH)_2$ nanosheets on nitrogen-doped carbon nanotubes network as high-performance electrocatalyst for oxygen evolution reaction. *J Alloys Compd* 2018;731:766-73. DOI

46.   Zhuang S, Tong S, Wang H, et al. The P/NiFe doped $NiMoO_4$ micro-pillars arrays for highly active and durable hydrogen/oxygen evolution reaction towards overall water splitting. *Int J Hydrogen Energy* 2019;44:24546-58. DOI

47.   Li YK, Zhang G, Lu WT, Cao FF. Amorphous Ni-Fe-Mo suboxides coupled with Ni network as porous nanoplate array on nickel foam: a highly efficient and durable bifunctional electrode for overall water splitting. *Adv Sci (Weinh)* 2020;7:1902034. DOI PubMed PMC

48.   Zhang H, Li X, Hähnel A, et al. Bifunctional heterostructure assembly of NiFe LDH nanosheets on NiCoP nanowires for highly efficient and stable overall water splitting. *Adv Funct Mater* 2018;28:1706847. DOI

49.   Wang F, Ma K, Tian W, et al. P-Doped $NiMoO_4$ parallel arrays anchored on cobalt carbonate hydroxide with oxygen vacancies and mass transfer channels for supercapacitors and oxygen evolution. *J Mater Chem A* 2019;7:19589-96. DOI

50.   Anjaneyulu U, Pattanayak DK, Vijayalakshmi U. Snail shell derived natural hydroxyapatite: effects on NIH-3T3 cells for orthopedic applications. *Mater Manuf Process* 2015;31:206-16. DOI